Journal of Petroleum Science and Engineering 210 (2022) 110053

Contents lists available at ScienceDirect

Journal of Petroleum Science and Engineering

journal homepage: www.elsevier.com/locate/petrol

Investigation of pore-throat structure and fractal characteristics of tight sandstones using HPMI, CRMI, and NMR methods: A case study of the lower Shihezi Formation in the Sulige area, Ordos Basin

Yuping Wu [a,b], Chenglin Liu [a,b,*], Siqi Ouyang [a,b], Bin Luo [c], Dingding Zhao [a,b], Wei Sun [d], Rizwan Sarwar Awan [a,b], Zhendong Lu [a,b], Guoxiong Li [a,b], Qibiao Zang [a,b]

[a] State Key Laboratory of Petroleum Resources and Prospecting, China University of Petroleum, Beijing, 102249, China
[b] College of Geosciences, China University of Petroleum, Beijing, 102249, China
[c] Research Institute of Exploration and Development, PetroChina Changqing Oilfield Company, Xi'an, 710018, China
[d] Department of Geology, Northwest University, Xi'an, Shanxi, 710069, China

ARTICLE INFO

Keywords:
Tight sandstone
Pore-throat structure
Fractal characteristics
Shihezi formation

ABSTRACT

The evaluation of pore-throat structure is essential for the exploration and exploitation of tight oil and gas reservoirs. In this study, various experiments such as casting thin section (CTS), scanning electron microscope (SEM), mercury intrusion porosimetry (MIP), and nuclear magnetic resonance (NMR) are used to investigate the pore-throat structure and fractal characteristics of the tight sandstone from the Permian Shihezi Formation in the Sulige area, Ordos Basin. The type and size of tight sandstone pores and throats are qualitatively analyzed by using CTS and SEM. However, the structural parameters such as the size and distribution of tight sandstone pores and throats are quantitatively calculated by HPMI, CRMI, and NMR. According to the advantages and disadvantages of each method, the HPMI and NMR are combined to characterize the full-size pore-throat distribution (PSD) of tight sandstone. Based on the fractal theory, the fractal dimensions (D) of pore-throat of tight sandstone are evaluated by HPMI, CRMI, and NMR.

The result shows the pores in the tight sandstone are mainly residual intergranular pores, dissolution pores, and inter-crystalline pores. There are few micro-cracks developed, and the throats are mainly tubular and curved sheets. The full-size PSD curve of tight sandstone presents the characteristics of the bimodal and unimodal distribution. It has a good agreement with petrophysical properties and movable fluid saturation. Different experimental methods can get different D. HPMI and NMR have different detection ranges and diverse principles for pore-throat evaluation, making sandstone's diverse fractal characteristics. The CRMI is more representative for studying the fractal characteristics of the throat. Moreover, there are two different types of throats: large throat and small throat. These throats have a double fractal feature. The relationship between D and the physical properties analyzes the parameters of the pore-throat structure, suggesting larger the D, the worse the physical properties of the reservoir. The development of the throat (especially the larger throat) controls the storage and fluid flow-ability of tight sandstone reservoirs. Mercury saturation, movable fluid saturation, and D are negatively correlated, indicating that the complicated pore-throat structure will reduce permeability and destroy the free fluid storage space.

1. Introduction

Tight gas is an important unconventional hydrocarbon resource, widely distributed around the world. These resources are very significant because these resources can overcome the need for global energy demand (Dai et al., 2017; Oluwadebi et al., 2019; Zhao et al., 2014; Zou et al., 2012). China is rich in tight gas resources that are approximately $21.85 \times 10^{12} m^3$ (Sun et al., 2019). Unlike conventional hydrocarbon reservoirs, tight sandstone has a complex microstructure, strong heterogeneity, multi-scale pore-throat sizes, and complicated pore-throat combinations (Clarkson et al., 2012; Li et al., 2018b). The pore-throat structures are significant to the storage capacity and fluid flow-ability

* Corresponding author. State Key Laboratory of Petroleum Resources and Prospecting, China University of Petroleum, Beijing, 102249, China.
E-mail address: liucl@cup.edu.cn (C. Liu).

https://doi.org/10.1016/j.petrol.2021.110053
Received 18 September 2021; Received in revised form 2 December 2021; Accepted 13 December 2021
Available online 16 December 2021

of tight sandstone reservoirs. It controls the productivity distribution and exploitation effects of petroleum reservoirs (Golab et al., 2010; Huang et al., 2018a; Qu et al., 2020). Therefore, the identification of microstructures in tight sandstone is significant for revealing the migration and storage mechanisms of tight gas (Clarkson et al., 2013; Li et al., 2017; Nie et al., 2021).

Currently, many technical approaches have been applied to study the microstructure of tight sandstone, including imaging observation technologies, fluid invasion technologies, and radiation detection technologies (Guo et al., 2019; Li et al., 2019). The morphological characteristics and pore-throat connectivity in tight sandstone can be directly observed using CTS, SEM, and CT scanning (Mayo et al., 2015; Ren et al., 2019; Zou et al., 2012). The fluid invasion methods can quantitatively characterize the characteristics of the pore, throat volume and size distribution, including CO_2 adsorption, N_2 adsorption, HPMI, and CRMI (Clarkson et al., 2013; Huang et al., 2018b, 2020a; Li et al., 2019; Nooruddin et al., 2014). Additionally, small-angle scattering and NMR can also quantitatively study the pore structure of unconventional reservoirs (Clarkson et al., 2012; Huang et al., 2020b; Zhang et al., 2019). However, all testing techniques have their advantages and limitations in studying the microstructure of sandstone (Nie et al., 2021; Qu et al., 2020). Fractal geometry, originally used to study irregular but naturally self-similar shapes, an effective tool for quantitative characterization of complexity (Mandelbrot, 1983). The pore throat structure and its fractal characteristics in the tight sandstone reservoir are naturally complex systems. Therefore, the fractal theory has been extensively used to study the complexity of the microstructure of sandstone (Li, 2010; Li et al., 2017; Zhang and Weller, 2014). It builds an effective bridge between the microscopic characteristics and the physical properties of tight reservoirs (Hu et al., 2012). The fractal dimension (D) is a crucial indicator to elaborate the heterogeneity of the microscopic structure. It has been used to study the pore-throat structure of tight sandstone (Li et al., 2017). With the increase of protrusions and depressions, the surface and structure of the pore-throat become rougher

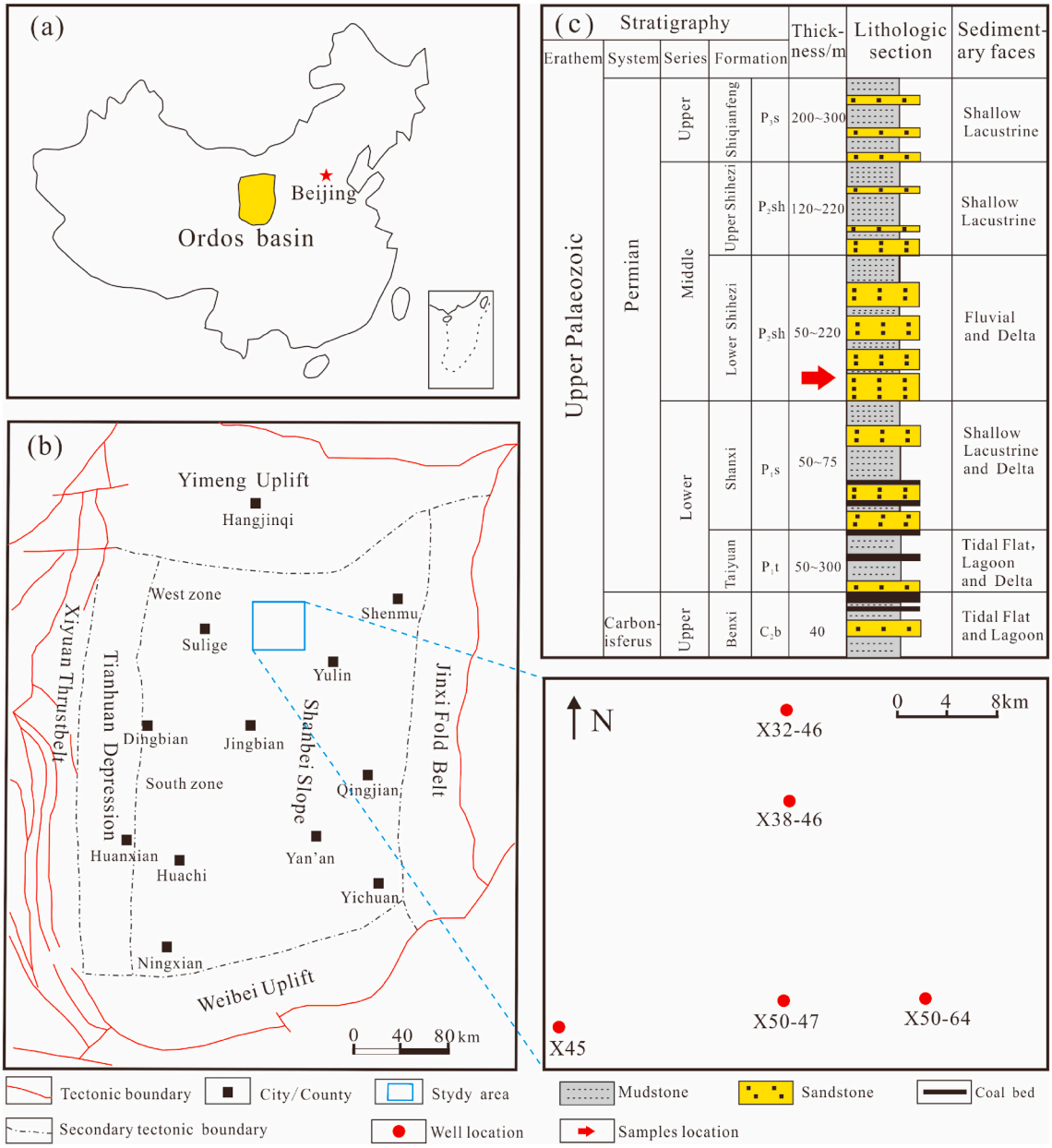

Fig.1. (a) Location map of the Ordos Basin, (b) Location map of structural units and wells in research area, and (c) stratigraphic column of Upper Paleozoic in the Sulige area (modified after Dai et al., 2017).

and more complex (Wang et al., 2014). The D can quantify the roughness of the material's surface. Usually, the D of sandstone is between 2.0 and 3.0 (Li and Horne, 2006). The increase of the D indicates the discrete distribution of pore-throat and poor connectivity (Li et al., 2017). Thus, the D is a great and effective index to elaborate the pore-throat characteristics (Li et al., 2017, 2019; Nie et al., 2021; Zhang and Weller, 2014).

In the Ordos Basin, the Shihezi Formation prior to becoming a tight sandstone reservoir has undergone complex sedimentary evolution and diagenetic alteration (Fan et al., 2019; Liu et al., 2019; Wang et al., 2017; Wu et al., 2021). In this study, the He8 member from the Sulige area has been taken as a research interest to study microstructure and fractal characteristics of tight sandstone reservoirs. The main goals of this article include: (1) Characterizing the tight sandstone pore-throat morphology and size distribution by CTS, SEM, HPMI, CRMI, and NMR; (2) Combining HPMI and NMR to quantitatively describe the full-size distribution of tight sandstone; (3) Clarifying the relationship between D, and physical properties, pore-throat structure parameters.

2. Geological setting

The Ordos Basin is a petroliferous basin located in the central part of China, with an area of about $25 \times 10^4 km^2$ (Fig. 1a) (Zhao et al., 2014). It belongs to a polycyclic craton basin with a very stable structural setting (Li et al., 2017; Yang and Liu, 2014; Zhao et al., 2014). The basin comprises six tectonic units: the Yimeng Uplift, Xiyuan Thrust Belt, Tianhuan Depression, Shanbei Slope, Jinxi Fold Belt, and Weibei Uplift (Fig. 1b) (Liu et al., 2019; Zhao et al., 2014). The Sulige Gas Field is located in the north-central Shabei slope, with an exploration area of $4 \times 10^4 km^2$ (Yang et al., 2015). The average burial depth of the tight gas reservoir is about 3000 m, and the geothermal gradient is approximately 30.3 °C/km (Fan et al., 2019; Yang et al., 2014). Previous studies indicated the formation pressure was between 24.19 MPa and 27.8 MPa, and the average lithostatic pressure coefficient was 0.86 (Yang et al., 2014). The study area is situated in the eastern part of Sulige Gas Field, rich in natural gas resources.

The Late Paleozoic sedimentary facies are evolved from marine to continental facies affected by the Hercynian movement. The early Benxi Formation, Taiyuan Formation, and Shanxi Formation were mainly continental surface sea deposits. In the late depositional period of the Shanxi Formation, it gradually transitioned to coastal and shallow delta deposits during the slow regression process. Eventually, tidal flats or swamps and peat accumulation occurred, forming a large area of the stable coal seam (Yang et al., 2015). These widely distributed coal-bearing formations in the basin have become high-quality source rocks, greatly enriching the tight gas resources. The main gas-producing layers in the basin are the Shanxi Formation and the Shihezi Formation (Fan et al., 2019; Nie et al., 2021). The Shihezi Formation can be further divided into eight subunits from top to bottom, namely He1 to He8, with a total thickness of 100–450 m (Dai et al., 2017; Hui et al., 2020; Zhao et al., 2014). Among them, the He8 member is the main gas-producing zone. According to previous research, this set of rocks belongs to braided river delta deposits (Hui et al., 2020; Xiao et al., 2019). Moreover, He8 member has poor reservoir quality, strong heterogeneity and is considered a typical tight sandstone.

3. Samples and methods

3.1. Samples

In this research, seven sandstone samples are selected from five wells located in the Sulige Gas Field (Fig. 1c). All samples are from the He8 member of the Lower Shihezi Formation. The burial depth of the samples is lower than 2900 m. The sandstone has undergone strong compaction, cementation and is characterized by compactness and strong heterogeneity.

3.2. Experimental measurements

All samples need to be cleaned of residual oil in rock pores before testing. It is usually washed with dichloromethane and distilled water and dried. All samples are separated into two parts. The smaller part is used for CTS and SEM experiments. The rest of the regular plunger samples are tested and analyzed for physical properties, and then HPMI, CRMI, and NMR experiments are performed.

3.2.1. Physical properties analysis

The porosity of the samples is evaluated by incorporating the Porerm-200 instrument, and the core porosity is measured using helium as a carrier gas. The permeability is measured using the STY-2 gas permeability tester using helium as a carrier gas.

3.2.2. XRD

XRD analysis is performed using a D2 Phaser diffractometer. 5 g of the sample is taken, ground to 300 mesh, and smeared on a glass slide for experimentation. The measurements and analysis are performed after setting the experimental parameters of the device. Before separating the clay fraction, 15% acetic acid is used to remove the easily soluble carbonate and then continuously washed with deionized water. Stokes' law is applied to separate the clay fraction from the stabilized aqueous suspension (Ufer et al., 2008). Then the paste is smeared on a glass slide to analyze the clay fraction after drying.

3.2.3. CTS and SEM

The CTS and SEM observations of the samples are completed by using LEEI DMRXHC and Quanta 200 F SEM system. The samples are ground into thin slices with a thickness of 0.03 mm and pasted on slides for observation. A cube sample with sides of 1 cm is used for SEM analysis to characterize the type and morphology of the pores-throat at the micro-nano scale. Before the observation, the surface of the shale sample is coated with gold to increase the conductivity (Curtis et al., 2012). The experimental temperature and the ambient humidity were 24 °C, and 40%, respectively.

3.2.4. HPMI

The HPMI experiment incorporated an Auto Pore IV 9520 instrument, with pressure ranges from 0 to 206.7 MPa, and the smallest measurable aperture is about 3.6 nm. The pore throat radius (r) of sandstone could be calculated using the following equation proposed by Washburn (1921):

$$P_c = \frac{2\sigma \cos\theta}{r} \quad (1)$$

Where: P_c is the capillary pressure, MPa; σ is the surface tension, N/m; θ is the wetting angle, °. Usually, $\sigma = 0.48$ N/m, $\theta = 140°$.

3.2.5. CRMI

The constant-speed mercury intrusion is carried out using the ENPG001 automatic pore detection system. In this method, pores and throats are identified through pressure fluctuations during mercury injection (Morrow Norman, 1970; Washburn, 1921; Yuan and Swanson, 1989). Due to the limitation of experimental conditions, the maximum injection pressure is 6.2055 MPa, and the detectable radius is about 120 nm. The experiment complies with the Chinese national standard GB/T 21650.1–2008.

3.2.6. NMR

The NMR RecCore 2500 equipment is used in this study at the Chinese Academy of Sciences. Set the following parameters for the device: the resonance frequency (2.38 MHz), the number of echoes (2048), the number of scans (128), the waiting time (5000 ms), and the echo interval (0.6 ms). Tight sandstone has three relaxation mechanisms:

particle surface, bulk fluid, and molecular diffusion relaxation(Kleinberg and Horsfield, 1990). The relaxation time of bulk fluid and molecular diffusion can be ignored when the samples are saturated with water (Huang et al., 2020b; Kleinberg and Horsfield, 1990). Thus, the relaxation time of T_2 can be simplified as:

$$\frac{1}{T_2}=\rho_2\frac{S}{V} \tag{2}$$

Where: T_2 is the surface relaxation time, ms; S/V is the specific surface area, μm^{-1}; and ρ_2 is the surface relaxivity (μm/ms).

Before the NMR experiment, the plunger-shaped sample needs to be vacuumed for at least 24 h and fully saturated with a calcium chloride solution with a concentration of 60,000 mg/L.

3.3. Methodology

3.3.1. NMR and mercury intrusion fitting method

The NMR signal can reflect the information of the microstructures. The mercury intrusion porosimetry (MIP) can obtain the pore-throat radius (r) of the sample. Thus, the T_2 can be converted into r by establishing the mathematic relation between T_2 and r (Zhang et al., 2019). Reservoirs with a complex pore-throat structure usually have a nonlinear relationship between S/V and the r (Huang et al., 2018b). Previous studies indicated the T_2 has an exponential relationship with the pore radius (Li et al., 2015):

$$T_2=\frac{r^n}{\rho_2 F_S} \tag{3}$$

Where: F_S is a dimensionless factor of the pore shape; n is the power exponent, dimensionless.

Define:

$$C=\frac{1}{\rho_2 F_s} \tag{4}$$

Eq. (4) can be written:

$$r_t=CT_2^{1/n} \tag{5}$$

Thus, the T_2 value of the sample can be transformed into r by calculating C and n. The principle of calculating C and n is shown in Fig. 2, and the specific operation process can be referred to in the literature (Huang et al., 2018b; Li et al., 2015; Zhang et al., 2019).

3.3.2. Fractal dimensions

3.3.2.1. Fractal dimensions from MPMI and CRMI. Many models for calculating the fractal dimension by MIP have been proposed (Brooks and Corey, 1964; Friesen and Mikula, 1987; Li, 2010; Shen et al., 1995). The fractal dimension calculation in this study adopts the capillary tube model (Huang et al., 2018a; Peng et al., 2019). The simplified mathematical relationship can be expressed as:

$$S_{Hg}(>r)=\frac{r_{max}^{3-D_m}-r^{3-D_m}}{r_{max}^{3-D_m}} \tag{6}$$

$$\lg\left(1-S_{Hg}(>r)\right)=(3-D_m)\lg(r)-(3-D_m)\lg(r_{max}) \tag{7}$$

Where: D_m is the "D" from MIP, S_{Hg} is the mercury saturation,%; r_{max} is the maximum pore-throat radius in μm. The D_m can be obtained by drawing the curve in the double logarithmic coordinates of lg(1-S_{Hg}) and lg(r), by fitting the slope of the curve K_m (K_m = 3-D_m) to obtain:

$$D_m=3-K_m \tag{8}$$

3.3.2.2. Fractal dimensions from NMR. NMR experiments can also characterize pore-throat morphological features (Dong et al., 2015; Guo et al., 2019). Considering the comparability between MIP and NMR experiments results, it is believed the pores and throats obtained by NMR also conform to the tubular model. Zhang and Weller (2014) used NMR T_2 spectral curve to study the fractal dimension of sandstone pore-throat structure and established a corresponding mathematical model.

$$V_c=\frac{V(<r)}{V}=\frac{T_2^{3-D_n}-T_{2\,min}^{3-D_n}}{T_{2\,max}^{3-D_n}-T_{2\,min}^{3-D_n}} \tag{9}$$

It is generally considered the T_{2min} is sufficiently smaller than most T_2 values, and it can be ignored. Therefore, the following two equations can be obtained:

$$V_c=\frac{T_2^{3-D_n}}{T_{2\,max}^{3-D_n}} \tag{10}$$

$$\lg(V_c)=(3-D_n)\lg(T_2)-(3-D_n)\lg T_{2\,max} \tag{11}$$

Where: D_n is the "D" from NMR; V_c is the cumulative pore volume; T_{2max} is the maximum transverse relaxation time; T_{2min} is the minimum transverse relaxation time. From Eq. (11), the curve slope K_n in the double logarithmic coordinate system can be obtained, and the D_n can be acquired as follows:

$$D_n=3-K_n \tag{12}$$

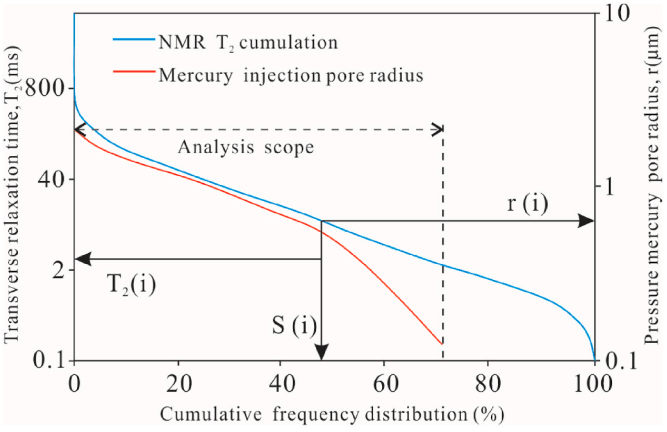

Fig. 2. The principle of conversion from T_2 to r.

4. Results

4.1. Mineral compositions and petrophysical properties

The physical properties and the XRD experimental results of the seven studied samples are presented in Table 1. The porosity of the He8 reservoir is between 6.50% and 18.30% (averaging 11.58%), and the permeability ranges from 0.07 to 0.46mD, averaging 0.25mD. However, there is a good positive correlation between porosity and permeability (R^2 = 0.701) (Fig.3). The samples are mainly enriched in quartz, ranging from 60% to 76%, with an average of 68.6%. Feldspar is very rare and only observed in sample #2. Calcite is present in most samples, but the content is very low. No traces of dolomite is found in all samples. The clay minerals mainly consist of illite and kaolinite, with an average of 44.64% and 32.24%, respectively.

4.2. Pore-throat types

Pores are important storage spaces, while throats are important seepage channels for fluids in tight sandstone reservoirs (Liu et al., 2021; Zhang et al., 2020). CTS and SEM images show that there are mainly three types of pores developed, including residual intergranular pores

Table 1
Petrophysical properties and mineral composition of the He8 member.

Sample	Well name	Depth (m)	Φ_{He} (%)	K_{He} (mD)	Mineral composition from XRD (%)					Relative abundance of clay minerals (%)			
					Qua.	Fel.	Cal.	Sil.	Clay	Ill.	Kao.	Chl.	I/S
#1	X45	3131.1	8.89	0.10	68.6	/	1	5	7.22	19.02	42.19	30.08	8.71
#2	X45	3137.2	15.52	0.45	76.0	1	/	4	4.15	58.25	5.09	21.98	14.68
#3	X32-46	2989.3	18.30	0.46	68.0	/	/	/	13.57	68.36	12.11	1.99	17.54
#4	X38-46	3026.2	10.41	0.07	68.0	/	1	1	4.48	54.71	2.97	30.18	12.14
#5	X50-47	3106.3	6.50	0.15	60.0	/	1	2	10.32	67.81	23.48	/	8.71
#6	X50-47	3108.2	11.75	0.39	69.0	/	1	7	8.29	18.5	71.45	/	10.05
#7	X50-64	2907.2	9.73	0.13	70.0	/	1	6	9.09	25.85	68.39	/	5.76

Note:Qua(Quartz); Fel(Feldspar); Cal(Calcite); Sil(Silicious); Ill(Illite); Kao(Kaolinite); Chl(Chlorite); I/S mixed-layer.

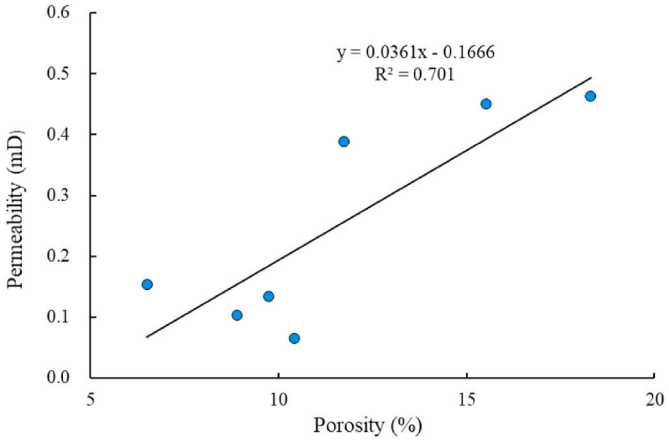

Fig.3. Relationship between permeability and porosity.

(Fig.4a), dissolution pores (Fig. 4a-b), inter-crystalline pores (Fig. 4d-f), and a few micro-cracks (Fig. 4g-h). Residual intergranular pores are formed by mechanical compaction and cementation of primary intergranular pores. They are irregular in shape and often coexist with chlorite film or secondary enlargement of quartz, and their pore size is greater than 50 μm (Fig.4a). Dissolution pores are dominated by lithic dissolution pores (Fig.4b), and feldspar dissolved pores are extremely rare (Fig.4c). The dissolved pores are irregular, with a pore size between 1 μm and 50 μm, and they are often filled by clay minerals such as kaolinite and chlorite. Inter-crystalline pores are widely developed in clay minerals, mainly in illite, kaolinite, and chlorite inter-crystalline pores (Fig. 4d-f). The pore size is mostly less than 2 μm, and the connectivity is usually poor. The throat types mainly consist of the tubular throat (Fig.4h) and the curved sheet throat (Fig.4i). These small throats have complex distribution and poor connectivity, which greatly affects the fluid's seepage ability.

4.3. Pore–throat distribution characteristics

4.3.1. HPMI result

Table 2 shows the HPMI experiment results. In the samples, the entry pressure ranges from 0.12 MPa to 0.72 MPa, averaging 0.47 Mpa. The sorting coefficient of all samples is greater than 2, averaging 2.59. Fig.5 shows the HPMI curve characteristics of the seven samples. For samples with high porosity and permeability, it is not obvious that lower entry pressure and lower curve slope are often accompanied. Thus the reservoir quality cannot be evaluated simply by the HPMI curve characteristics. For example, the capillary pressure curve of sample #2 is significantly lower than other samples, reflecting that it has a part of larger pore throats that lower the entry pressure. However, it is observed that the mercury saturation gradually increases with an increase of pressure (maximum mercury saturation 93.89%). Reveals, although the internal pore-throat has a certain degree of connectivity, the sorting characteristic is not good, indicating the pore-throat has a strong heterogeneity. The physical properties of sample #3 are similar to sample #2, which has a maximum mercury saturation of 97.01% and larger entry pressure, but the sorting coefficient is significantly smaller. Therefore, it indicates the internal pore-throat heterogeneity is weak, making the efficiency of mercury withdrawal of sample #3 significantly greater than that of sample #2.

4.3.2. CRMI result

CRMI can accurately measure the key parameters that reflect the characteristics of microstructures in sandstone, including pore and throat radius distribution, pore-throat radius ratio distribution, etc (Zhang et al., 2019; Zhao et al., 2015). Fig.6 shows the typical mercury curve of sample #2, including three curves: the pores, throat, and total mercury saturation. In the early stage of mercury intrusion, the total mercury saturation is mainly controlled by the pores. As the pressure increases, the total mercury saturation is gradually controlled by the throat. Table 3 shows the results of CRMI. The entry pressure of the samples ranges from 0.346 MPa to 0.771 MPa, averaging 0.570 MPa. The pores and throat radius of the samples present a normal distribution, and the pore radius is in the range of 100–200 μm (Fig.7a). The throat radius ranges from 0.4 μm to 1.00 μm, averaging 0.72 μm (Fig.7b). Although the CRMI experiment can obtain the pore radius size, due to the limitation of the experimental principle, this is not a reflection of the real pore size (Qu et al., 2020). The maximum mercury injection pressure of CRMI is about 6.2 MPa, making the average maximum mercury saturation only 37.43%. It is much lower than the mercury saturation of HPMI, indicating a considerable portion of small pore throats ($r < 0.12$ μm) can not be detected because it exceeded its detection range.

4.3.3. NMR result

The NMR T_2 spectrum of fully saturated formation water can reflect the characteristics of the pore-throat structure of the sample (Dong et al., 2015; Qu et al., 2020). Fig.8 shows the T_2 spectrum of seven studied samples measured under fully water-saturated conditions, showing a unimodal or bimodal distribution. The T_2 value is between 0.01 ms and 1000 ms. Therefore, most of the samples present a unimodal distribution. Although some of the samples have bimodal characteristics (#4, #5, and #6), they are still characterized by the height of the left peak, which indicates that the pore-throat is small and physical properties are poor. At the same time, the 300psi centrifugation experiment is performed on these seven water-saturated samples. Moreover, the NMR experiment is performed again after the centrifugation. Generally, the NMR T_2 relaxation time spectrum of fully water-saturated and the after 300 psi centrifugation represent the states of saturated fluid and completely discharged fluid in the reservoir, respectively (Dong et al., 2015). Comparing the difference data of the NMR response amplitude and relaxation time in the two spectra, each sample's proportion of the movable fluid can be obtained (Yao et al., 2010). Fig.9 shows the method to calculate the T_2 cut-off value and the movable fluid content. Based on this principle, the T_2 cut-off value, movable fluid saturation, and movable fluid porosity are calculated in all samples. Table 4 shows

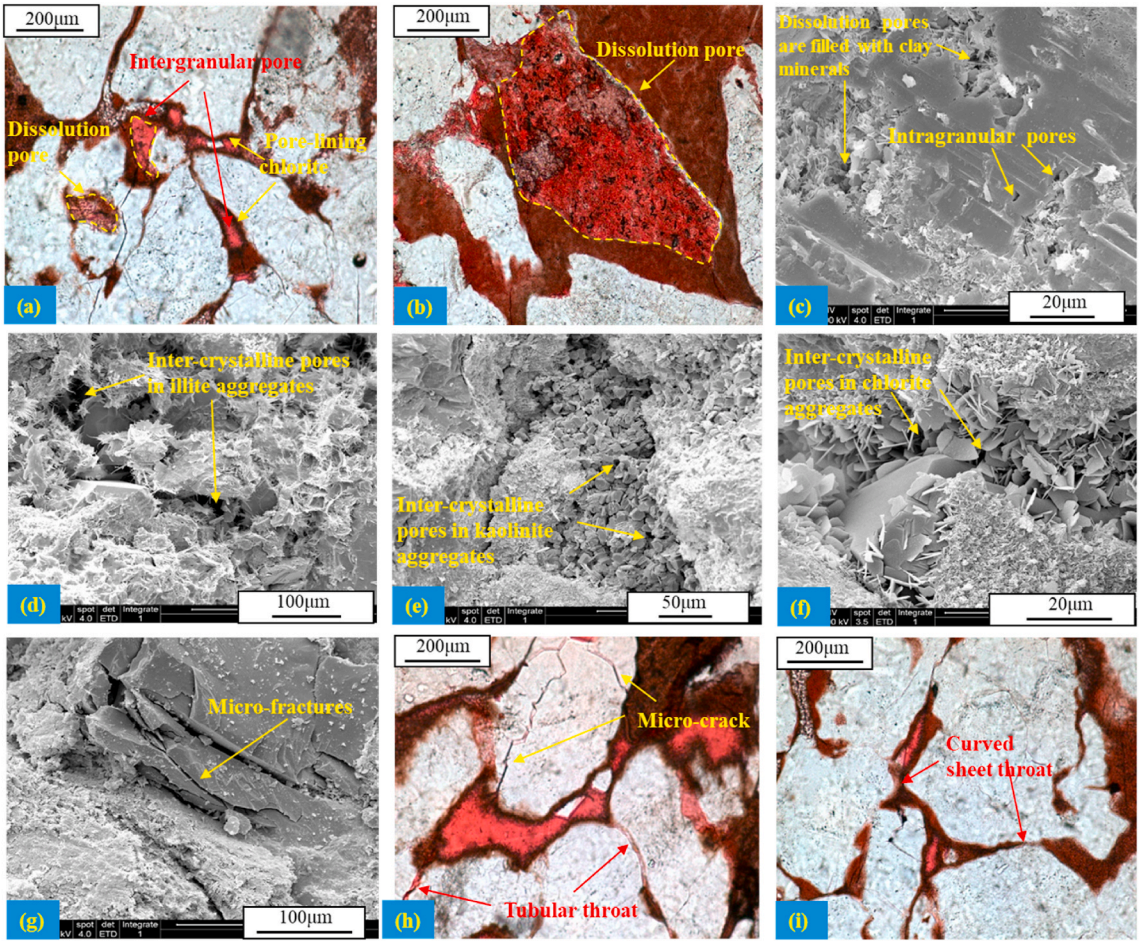

Fig.4. Thin section and SEM is showing the pore-throat types. (a) residual primary intergranular pores, dissolution pores; (b) dissolution pores formed in rock fragments; (c) intragranular dissolution micro-pores; (d) inter-crystalline pores; (e) kaolinite fill-up and a large number of inter-crystalline pores among authigenic minerals; (f) chlorite fill-up among authigenic minerals and inter-crystalline pores in chlorite aggregates; (g) micro-fractures around the rock particles; (h) tube-shaped throat; and (i) curved sheet throat.

Table 2
Characteristic of pore structure obtained by HPMI.

Sample	Well	Depth (m)	Entry pressure (MPa)	Median radius (μm)	Sorting coefficient	Maximum mercury saturation (%)	Efficiency of mercury withdrawal (%)
#1	X45	3131.1	0.72	0.193	2.000	92.00	40.37
#2	X45	3137.2	0.12	0.834	2.867	93.89	20.65
#3	X32-46	2989.3	0.47	0.104	2.163	97.01	40.11
#4	X38-46	3026.2	0.72	0.037	2.824	83.06	29.54
#5	X50-47	3106.3	0.45	0.103	2.944	83.43	29.78
#6	X50-47	3108.2	0.45	0.175	2.600	88.34	26.65
#7	X50-64	2907.2	0.46	0.277	2.379	92.74	27.77

the NMR experiment results of seven samples. The T_2 cut-off values are distributed in the range of 3.22–11.57 ms, averaging 7.12 ms. The movable fluid saturation obtains a low value (ranges from 5.38% to 32.68%, averaging 18.10%), reflecting the complexity of the micro-structure in tight sandstone.

4.3.4. The full-size pore-throat distribution

The HPMI experiment can directly obtain the distribution characteristics of pore-throat. However, it has many defects. For example, the minimum pore diameter measured at the maximum pressure of 200.25 MPa is 3.67 nm, and a considerable part of the tiny pore-throat in tight sandstone cannot be obtained. Moreover, high pressure can easily cause micro-cracks in the sample, making the test results inaccurate (Lai and Wang, 2015; Qu et al., 2020). The NMR is a non-destructive experiment, and the detection zone obtained are wider than those obtained by HPMI. It can study the pores and throat that HPMI cannot detect (Lai et al., 2018; Qu et al., 2020; Zhang et al., 2019). Thus, this research combines NMR and HPMI to form the full-size PSD of the samples. The method of converting the T_2 value of NMR into the pore-throat radius r has been described in the methodology part.

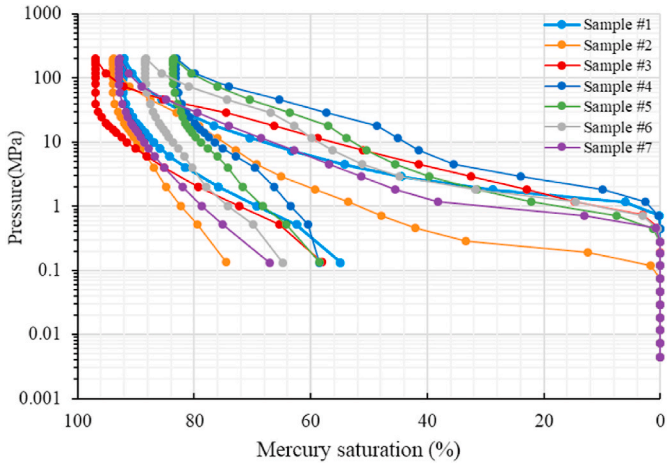

Fig.5. Typical HPMI curves.

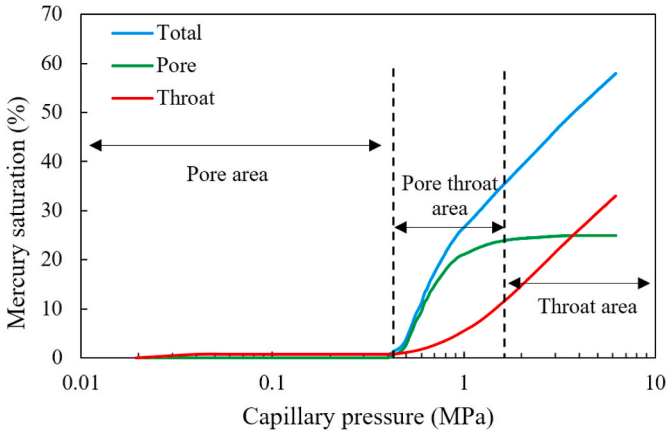

Fig.6. Typical CRMI curve.

The specific process of characterizing the full-size PSD of the sample is as follows. The T_2 and r are fitted under the same cumulative distribution frequency. It can be seen a distinct inflection point divides the curve into two-segment. For example, in sample #2 (Fig.10), a turning point appears when the r is about 1.915 μm. The least-square method is used to calculate the C and n of the two parts, and the results are presented in Table 5. Based on this, an empirical formula can be acquired to convert T2 and r for each sample. Then the r corresponding to the T_2 of the sample can be obtained. The full-size PSD of the seven samples is presented in Fig.11. The PSD curve is unimodal or bimodal, and the r mainly ranges from 0.001 to 10 μm. Sample #1 has a high right-peak and a narrow pore size distribution range, indicating a large pore-throat with serious heterogeneity, poor fluid seepage ability (with permeability 0.1 mD), and the low movable fluid content. Sample #3 shows a broad and gentle single peak, indicating both large and small pore-throat are distributed, while the heterogeneity is weak. The physical properties of sample #2 are similar to sample #3, but with a wider r distribution range and larger pore-throat size, making the connectivity of pore-throat better than that of sample #3. Samples #4 and #5 have obvious low left-peak and high right-peak characteristics, suggesting the large pore-throat are the main ones, and the overall pore-throat has a strong heterogeneity. The morphology of samples #6 and #7 is similar to sample #2. However, the r is mainly less than 2 μm, indicating a small pore-throat and better connectivity, relatively weak pore-throat heterogeneity, and a relatively high movable fluid saturation.

5. Discussion

5.1. Comparison of D calculated by different methods

Some scholars suggest the microstructure of tight sandstone has multi-fractal features when using the MIP method (Huang et al., 2018a; Lai and Wang, 2015; Li et al., 2017; Zhu et al., 2018). In addition, when applying HPMI experiments (with maximum pressure 413 MPa), it is believed the tight sandstone has triple-fractal characteristics (Li et al., 2017). The maximum pressure of the instrument applied in this experiment is 200.25 MPa, while the smallest pore diameter that can be measured is 3.67 nm. Fig.12 shows the relationship between Lg(1-S_{Hg}) vs. Lg(r) of sandstone samples. It is observed that the pore-throat fractal features of most samples have one stage (sample #3 has two obvious stages), reflecting the pore-throat structure does not have multi-fractal characteristics. Different pressures may cause this phenomenon. The per-unit balance time in the mercury injection process is different, and the number of mercury injection balance points used is different (Lai and Wang, 2015; Li, 2010).

Table 6 presents the fractal dimension calculated according to the MPI. The fractal dimension Dm calculated by the HPMI is between 2.6404 and 2.8233, indicating the pore-throat system has good fractal features. Except for sample #3, the fractal dimension fitting coefficient R^2 of the remaining six samples is between 0.9599 and 0.9970, with an average of 0.9782. Sample #3 has obvious two-segment characteristics, the fractal dimension of the left segment D_{m1} = 2.0157, and the right segment D_{m2} = 2.737, suggesting the pore-throat structure of this sample has double-fractal features.

The fractal dimension of sandstone obtained by HPMI reflects the comprehensive self-similarity characteristics of pores-throat to some extent. However, it cannot distinguish the fractal features of pores and throats. Huang et al. (2018a, b) have calculated the D of pores and throats using the CRMI experiment (Huang et al., 2018a). However, because the pore size of the CRMI is obtained according to the equivalent sphere model, it means the pore radius and pressure do not have a

Table 3
Characteristic of pore structure obtained by CRMI.

Sample	Well	Depth (m)	Entry pressure (MPa)	Average pore radius (μm)	Average throat radius (μm)	Pore volume (cm^3/g)	Throat volume (cm^3/g)	Mercury saturation (%)
#1	X45	3131.1	0.627	152.57	0.79	1.72	4.04	19.26
#2	X45	3137.2	0.413	149.23	1.00	9.81	13.01	57.87
#3	X32-46	2989.3	0.346	153.31	0.87	6.71	10.55	38.93
#4	X38-46	3026.2	0.604	143.99	0.73	0.46	3.42	20.61
#5	X50-47	3106.3	0.572	142.41	0.70	3.27	11.87	39.26
#6	X50-47	3108.2	0.771	164.43	0.54	10.11	9.54	53.91
#7	X50-64	2907.2	0.657	154.28	0.42	0.27	0.46	32.17

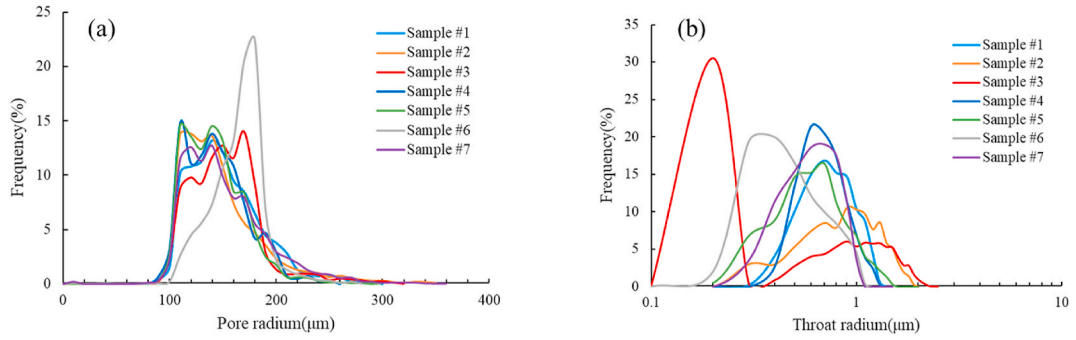

Fig.7. The characteristic of pore and throat radius from CRMI.

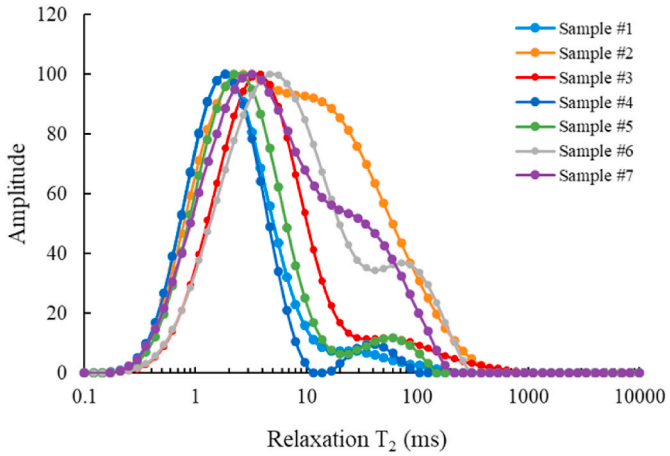

Fig.8. The T_2 spectra of the samples.

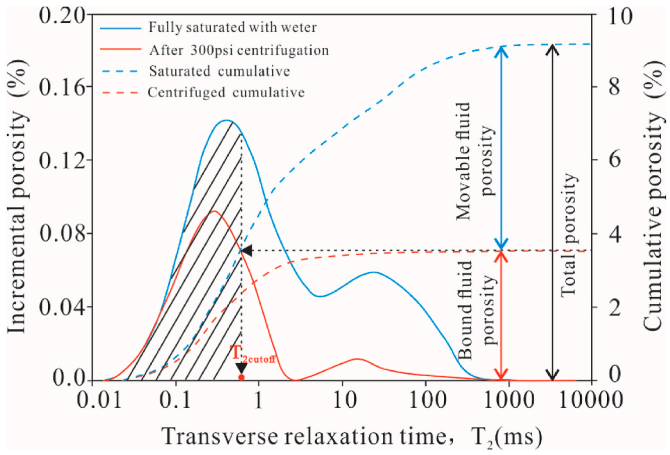

Fig.9. Principle of calculating the T_2 cutoff.

corresponding relationship, so the calculated pore size cannot reflect the actual pore size (Xiao et al., 2016; Zhao et al., 2015). Although in the relationship graph of $Lg(1-S_{Hg})$ vs. $Lg(r_p)$ (Fig.13a), the fitting curve of each sample presents an obvious three-segment. It doesn't reflect actual pores. Therefore, the following part mainly discusses the throat fractal dimension of tight sandstone.

Fig.13b shows the $Lg(1-S_{Hg})$ vs. $Lg(r_t)$ fitting curve of sample #6, which indicates the fractal features of the throat have two-segment characteristics. The left part with higher pressure corresponding to the fractal characteristics of the smaller throat identified as D_{m-t1}, and the right segment with lower pressure represents the larger throat identified

Table 4
Parameters from the NMR.

Sample	Well	Depth (m)	Porosity of movable fluid (%)	Movable fluid saturation (%)	$T_{2cutoff}$ (ms)
#1	X45	3131.1	0.73	8.48	3.2206
#2	X45	3137.2	4.91	32.67	8.0306
#3	X32-46	2989.3	2.25	13.78	11.5742
#4	X38-46	3026.2	0.58	5.38	3.8664
#5	X50-47	3106.3	0.91	8.02	5.5722
#6	X50-47	3108.2	1.55	25.84	9.6411
#7	X50-64	2907.2	3.17	32.54	7.9852

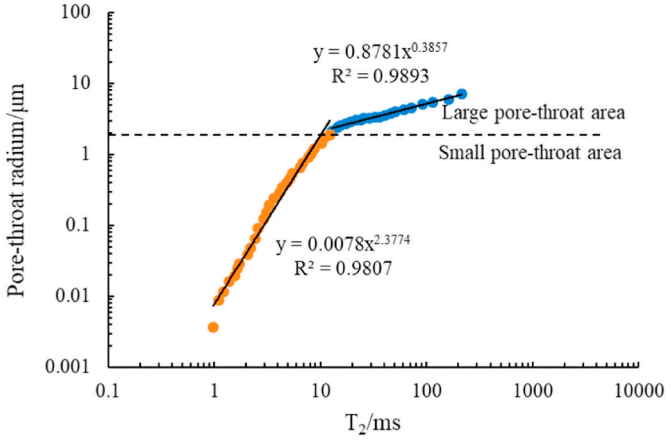

Fig.10. The relationship between T_2 and r of Sample #2.

as D_{m-t2}. Table 6 shows the statistical results of the throat fractal dimension of seven samples. Overall, the large throat fractal dimension (D_{m-t2}) ranges from 2.904 to 2.9777, and the correlation coefficient R^2 is between 0.9435 and 0.988. The small throat fractal dimension is between 2.8029 and 2.9925, and the fitting coefficient R^2 is between 0.9825 and 0.998. The demarcation point of self-similarity is between 312 nm and 602.5 nm, which has obvious irregularities. Comparing the D of the large and small throat demonstrates the D of the large throat is significantly larger, indicating the large throat's surface is rougher than that of the small throat. It may be related to the fact that the large throat is easier to develop lining-like clay minerals, making the throat more complicated.

The NMR T_2 spectrum can characterize the occurrence state of the fluid in the reservoir and reflect the reservoir's microstructure (Guo

Table 5
Conversion parameters between the T_2 and r.

Sample	Small pore-throat			Large pore-throat			Inflection radius(μm)
	C	n	R^2	C	n	R^2	
#1	0.0211	0.3526	0.9600	0.3031	3.7481	0.8845	0.3775
#2	0.0078	0.4206	0.9807	0.8781	2.5927	0.9893	1.9150
#3	0.0059	0.5267	0.9930	0.3056	4.0683	0.9652	0.4773
#4	0.0047	0.2980	0.9807	0.1833	2.8193	0.8758	0.2219
#5	0.0025	0.2826	0.9886	0.3722	3.1270	0.9364	0.4923
#6	0.0007	0.3791	0.9812	0.1171	2.3343	0.9774	0.2786
#7	0.0062	0.4402	0.9941	0.3080	2.5151	0.9820	0.5262

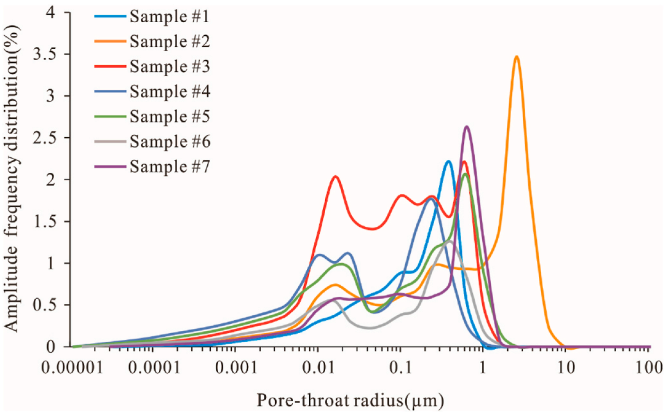

Fig.11. Full-size distributions of the samples.

et al., 2019; Huang et al., 2020b; Zhou et al., 2016). Zhang and Weller (2014) proposed a method to study the microstructure of sandstone using NMR and fractal theory (Zhang and Weller, 2014). This research utilized the same method to analyze sandstone samples. The cross plot of Lg(V) vs. Lg(T_2) based on NMR is presented in Fig.14. Since the $T_{2cutoff}$ divides the pore into seepage pores and adsorption pores, it can be used as an inflection point to divide the curve into two obvious linear segments, namely $T_2<T_{2cutoff}$ segment and $T_2>T_{2cutoff}$ segment (Dong et al., 2015; Peng et al., 2019). The corresponding fractal dimensions are called $D_{n\text{-}s}$ and $D_{n\text{-}l}$, respectively (Li et al., 2018b; Shao et al., 2017; Zhou et al., 2016). $D_{n\text{-}s}$ represents the fractal dimension of the specific surface area of the adsorption space corresponding to the shorter T_2 times, and $D_{n\text{-}l}$ represents the fractal dimension of the seepage space volume corresponding to the longer T_2 times (Guo et al., 2019; Li et al., 2018b; Zhou et al., 2016). The D of each sample using the NMR method is shown in Table 7. The $D_{n\text{-}s}$ of the $T_2<T_{2cutoff}$ segment is between 0.0592 and 0.4102, and the $D_{n\text{-}l}$ of the $T_2>T_{2cutoff}$ segment is 2.8206–2.9727. The correlation coefficient R^2 of $D_{n\text{-}l}$ is between 0.8762 and 0.9571, with an average of 0.9274. It is larger than $D_{n\text{-}s}$, which is between 0.7376 and 0.844, averaging 0.8203. The different coefficient shows the fluid seepage pore has more fractal characteristics than the adsorption pore (Guo et al., 2019). Some scholars suggest the surface roughness of the

Table 6
Fractal dimensions of samples based on MIP data.

Sample	D_m	R^2	$D_{m\text{-}t1}$	R^2	$D_{m\text{-}t2}$	R^2
#1	2.8233	0.9970	2.9237	0.9952	2.9777	0.972
#2	2.6404	0.9781	2.8029	0.9944	2.9536	0.9435
#3	D_{m1}/2.0157 D_{m2}/2.7370	0.9828 0.9767	2.9752	0.9911	2.9126	0.9813
#4	2.6824	0.9599	2.8876	0.9825	2.975	0.9706
#5	2.7152	0.9792	2.7967	0.992	2.9567	0.9725
#6	2.6559	0.9726	2.8275	0.998	2.904	0.988
#7	2.7747	0.9826	2.9925	0.982	2.964	0.971

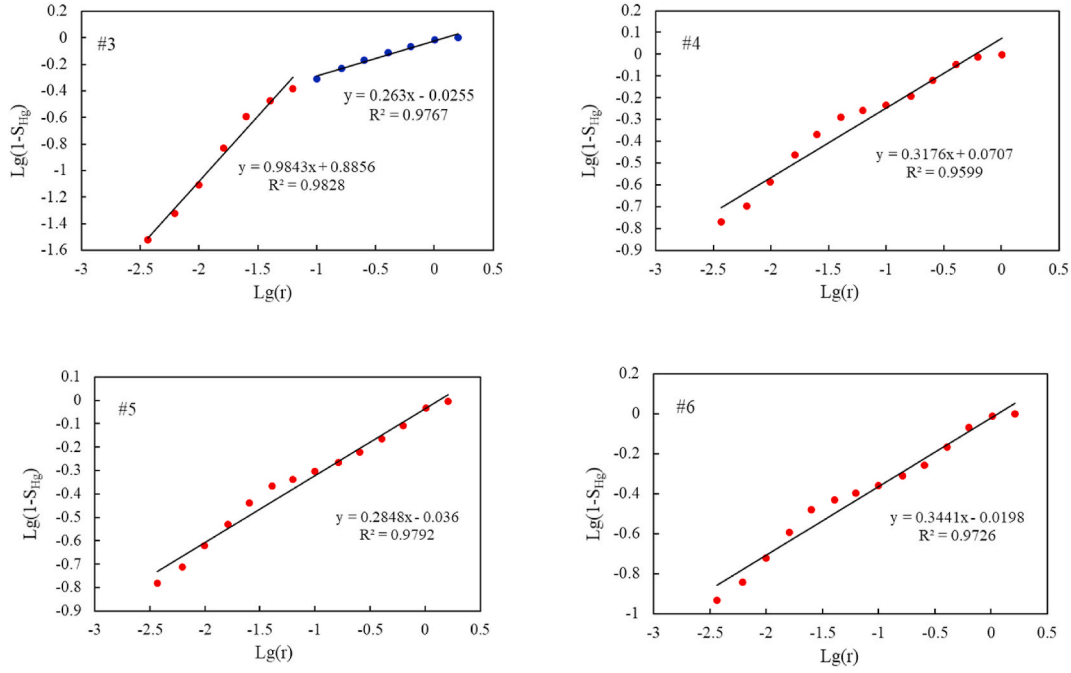

Fig.12. The cross plot of Lg(1-S_{Hg}) vs. Lg(r) based on the HPMI data.

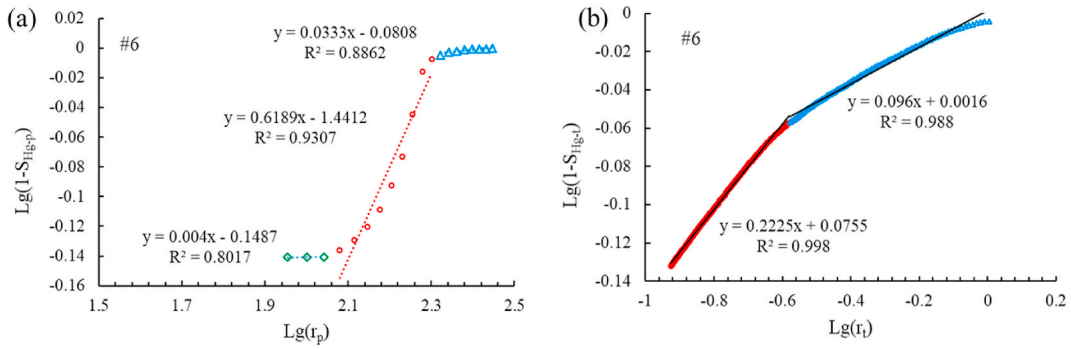

Fig.13. The cross plot of $Lg(1-S_{Hg})$ vs. $Lg(r_p)$ and $Lg(r_t)$, based on CRMI data.

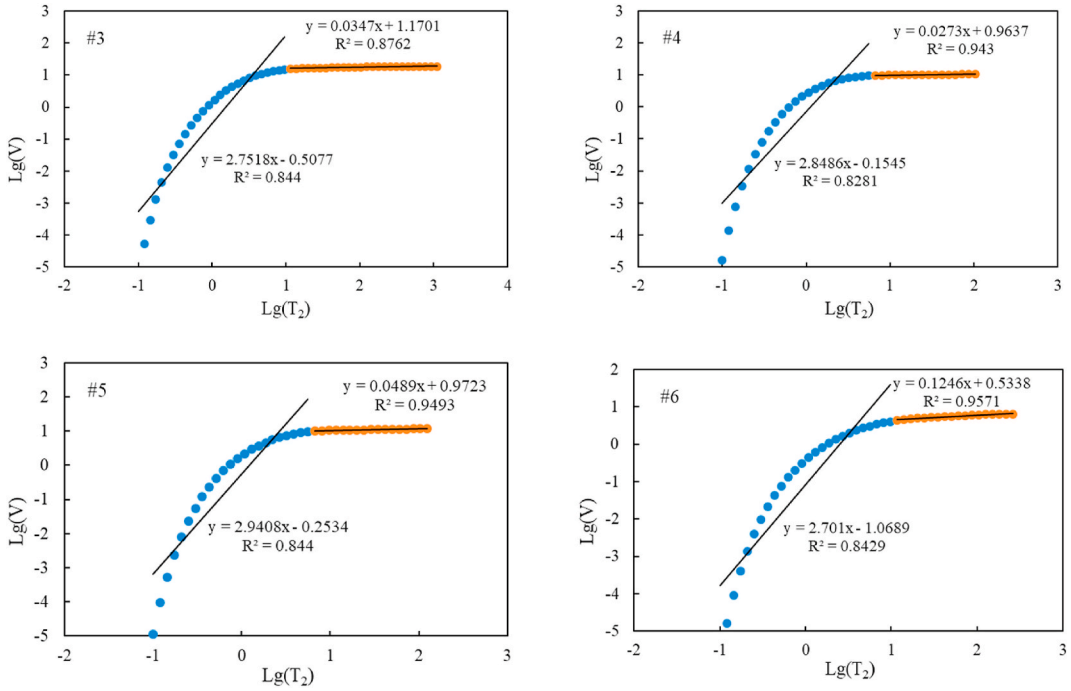

Fig.14. The cross plot of Lg(V) vs. $Lg(T_2)$ based on NMR. The blue and red circles indicate the T_2 value less and greater than the $T_{2cutoff}$. (For interpretation of the references to colour in this figure legend, the reader is referred to the Web version of this article.)

Table 7
Fractal dimensions of the samples based on NMR.

Sample	$T_2<T_{2cutoff}$		$T_2>T_{2cutoff}$	
	D_{n-s}	R^2	D_{n-l}	R^2
#1	0.1440	0.8293	2.9716	0.8914
#2	0.4102	0.8164	2.8206	0.9389
#3	0.2482	0.844	2.9653	0.8762
#4	0.1514	0.8281	2.9727	0.9430
#5	0.0592	0.844	2.9511	0.9493
#6	0.2990	0.8429	2.8754	0.9571
#7	0.2025	0.7376	2.8545	0.9361

micropore has a greater impact on the relaxation time than the specific surface area. Thus the D_{n-s} less than 2.0 reflects the structural characteristics and complexity of the micropore surface (Li et al., 2018a; Shao et al., 2017; Zhou and Kang, 2016).

The comparison of fractal dimensions in the studied samples calculated by HPMI, CRMI, and NMR shows the pore-throat structure of the tight sandstone has fractal characteristics. However, the D calculated by different methods is different. Many scholars have also observed this phenomenon using different physical models (Guo et al., 2019; Ma et al., 2019; Zhang et al., 2020; Zhu et al., 2018). The reason may be related to the experimental principles of different methods (Zhou and Kang, 2016). The HPMI characterizes the features of throats and their connected pores rather than the pores themselves. It reflects the changes in the connected pores of the reservoir and covers the fractal characteristics of pore throats ranging from nanometers to micrometers (Guo et al., 2019; Zhu et al., 2018). The CRMI can only better characterize the characteristics of the reservoir throat parameters. Therefore, the calculated fractal dimension reflects the throat characteristics. Moreover, previous studies have shown that the beginning of the mercury injection process is likely to cause data errors, affecting the calculation of fractal dimensions (Li, 2010; Schmitt et al., 2013). However, NMR uses the distribution of hydrogen nuclei in the fluid to acquire the size and distribution features of the pore-throat. This technique has a wider detection range, and its characterizable pore diameter is much smaller than the smallest pore throat that MIP can detect. Therefore, the NMR can more comprehensively characterize the features of the entire microstructure (Guo et al., 2019). The previous study pointed out the minimum aperture range required for fractal studies using nuclear magnetic T_2 spectra is from tens of nanometers to hundreds of nanometers (Ouyang et al., 2016). In

this case, the influence of bulk relaxation and diffusion relaxation cannot be ignored (Ouyang et al., 2016). Additionally, factors such as mineral constituents and magnetic material will also affect the accuracy of NMR experiments, which will affect the calculation of fractal dimension (Guo et al., 2019). On the other hand, the difference in MIP and NMR's fractal dimensions may be related to different fluid probe technologies (Zhu et al., 2018). Molecular probes (Hg and water) have different dynamic diameters (the size of mercury atoms and water molecules are 0.3 nm and 0.4 nm, respectively). Mercury can enter the pore space where water molecules cannot enter, and it will also have a significant impact on the results (Zhu et al., 2018). Therefore, the differences in the experimental results of different experiments are understandable. This research suggests the microstructure of tight sandstone in the Shihezi Formation has overall fractal characteristics. It does not have multi-fractal characteristics, while throats have double-fractal characteristics.

5.2. Relations between D and physical properties

Fractal dimension has a certain relationship with petrophysical properties (Guo et al., 2019; Qu et al., 2020; Zhu et al., 2018). Therefore, this research fitted D_m, $D_{m\text{-}t1}$, and $D_{m\text{-}t2}$ obtained by the MIP method with porosity and permeability. The results show a good negative correlation between D_m of pore-throat and physical properties (Fig.15a, b). The larger the D, the more complex the microstructure and the poor the petrophysical properties of the reservoir. There are obvious differentiation characteristics between $D_{m\text{-}t1}$, $D_{m\text{-}t2}$, porosity, and permeability (Fig. 15c-f). Among them, $D_{m\text{-}t2}$ has a significantly better correlation with porosity and permeability, suggesting the larger throat in the tight sandstone has a better contribution to the physical properties. The small throat has no significant influence on the physical properties of the reservoir; that is, the ability of the reservoir space to allow gas to pass through is mainly controlled by the smoothness of the large throat surface. However, when the gas or other fluid flows in the rock, it passes through a series of complex and changeable combinations of pore and throat. In this case, both pores and throats affect fluid flow. The effect of small pore throats on seepage capacity may be because bound water tends to accumulate in small pore throats, limiting the contribution of small pore throats to permeability. In general, the more developed the reservoir with a larger pore throat, the more favorable it is to develop tight sandstone gas.

5.3. Relationship between D and pore–throat structure parameters

The D is closely related to the microstructure of the reservoir (Li et al., 2017). Pore and throat volume, mercury saturation, and movable fluid saturation are used to fit with Dm-t1, Dm-t2, and Dn-l to study the relationship between the D and the microstructure parameters, the average pore and throat radius (Fig.16). The results indicate the pore and throat volume are negatively correlated with the D of the throat (Fig. 16a-d). In addition, $D_{m\text{-}t1}$ has a significant correlation with throat volume and $D_{m\text{-}t2}$. It has a conspicuous correlation with pore volume, suggesting the contribution of large and small throats to the reservoir space is different. The average pore radius does not correlate with $D_{m\text{-}t1}$ (Fig.16e), but it has a significant negative correlation with $D_{m\text{-}t2}$ (Fig.16f). It indicates smaller the D of the large throat, the weaker the heterogeneity, smaller specific surface area, and larger average pore radius. In other words, the size of the reservoir space is mainly affected

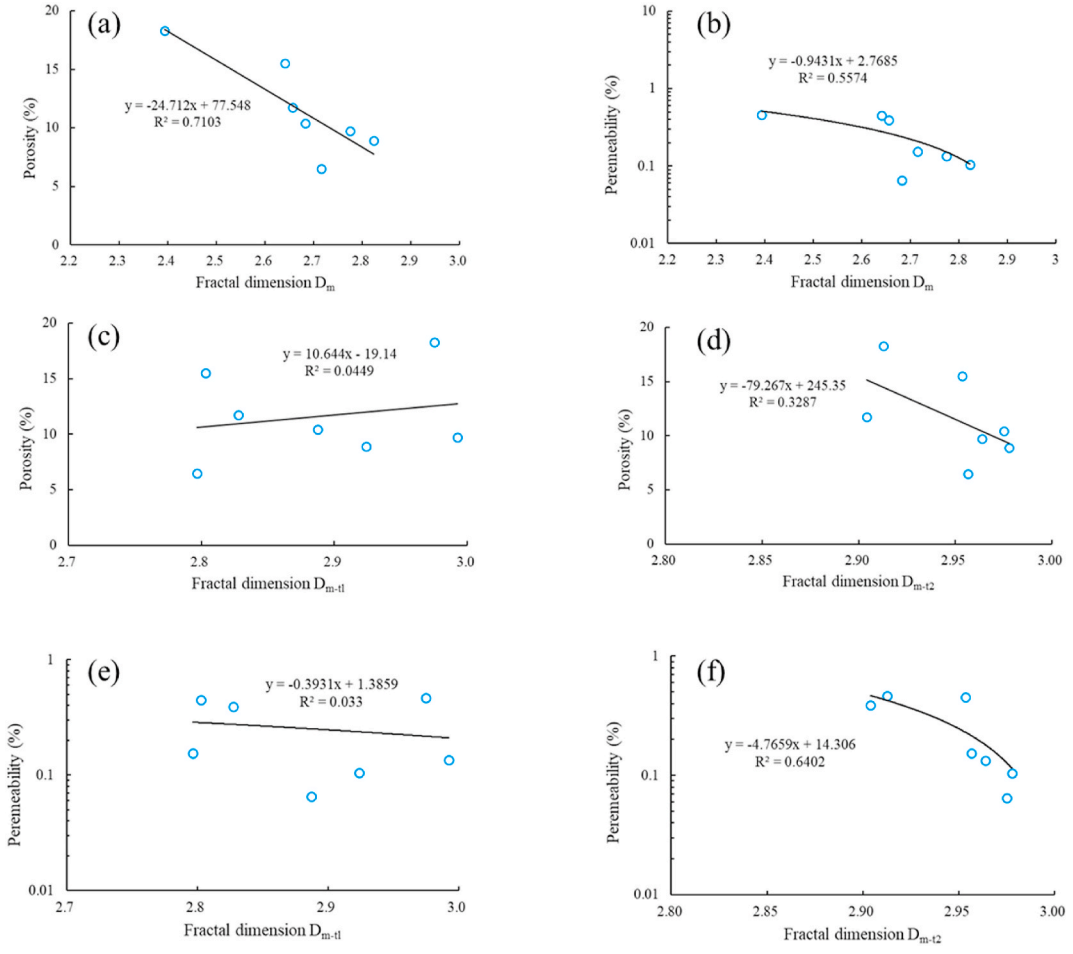

Fig.15. The plot of D_m, $D_{m\text{-}t1}$, and $D_{m\text{-}t2}$ vs. porosity (a)–(c) and permeability (d)–(f).

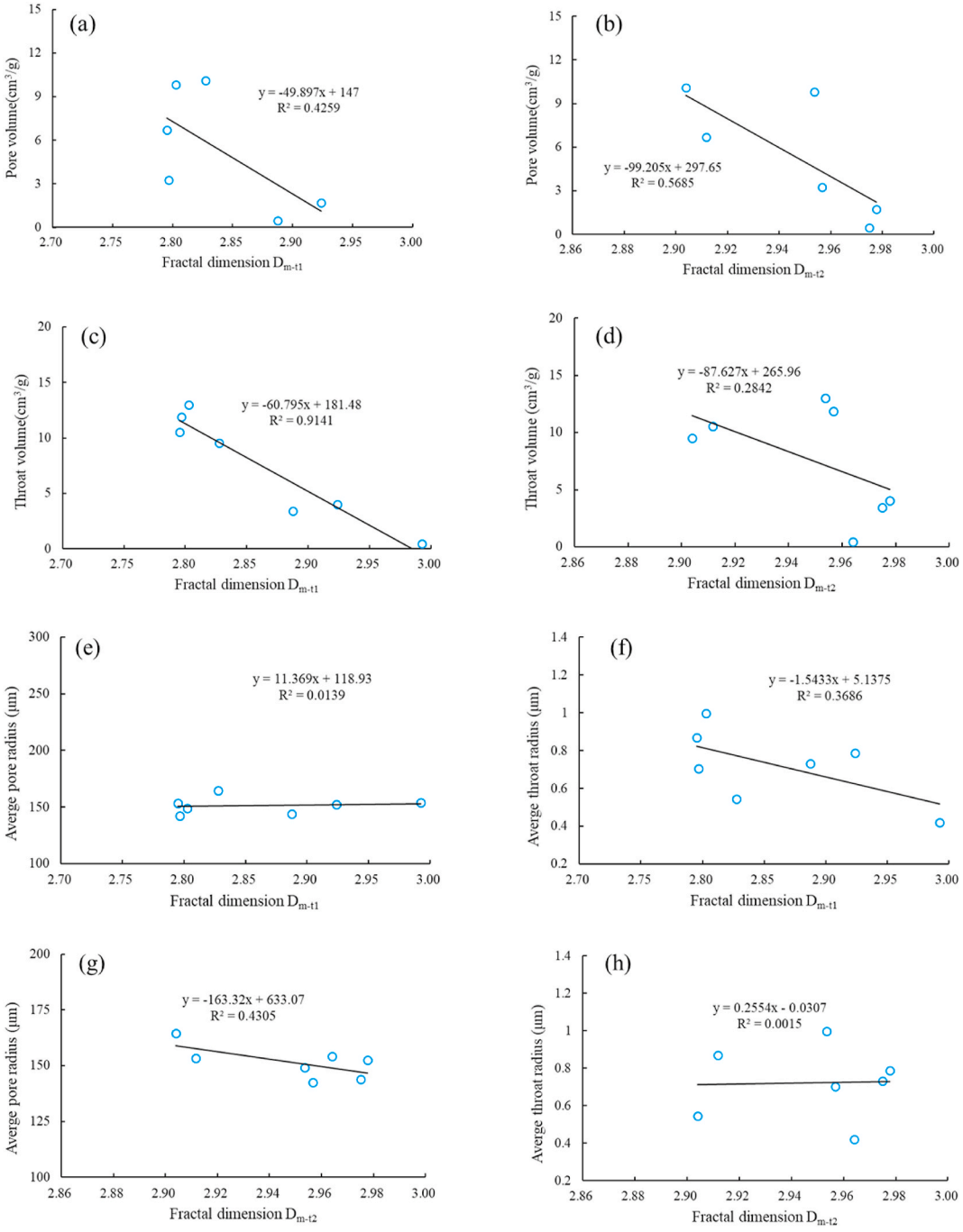

Fig.16. The plot of $D_{m\text{-}t1}$, $D_{m\text{-}t2}$ vs. pore-throat volume (a)–(d) and average pore-throat radius (e)–(h).

by the large throat. It means the more developed the large throat of tight sandstone, the stronger the reservoir capacity, and the easier it is to form the sweet spot of tight sandstone gas. On the contrary, the correlation between the average throat radius and $D_{m\text{-}t1}$ is significantly better than $D_{m\text{-}t2}$ (Fig. 16g, h). It is difficult to separate large throats from small pores due to the complex and diverse forms of pore-throat in tight sandstone. Small throats can represent the whole distribution characteristics of the reservoir throats. Therefore, the small throat has a closer relationship with the average throat radius. It indicates the development of the small throat controls the average throat size of the sample. When the average throat in the sandstone is smaller, the development of a small throat is relatively higher. Thus the pore throat of the tight sandstone is more complex, and the quality of the reservoir is worse.

Under the same termination pressure, the higher final mercury saturation indicates better reservoir quality (Qu et al., 2020). Fig.17a shows the final mercury saturation is negatively correlated with the D_m. It indicates the larger D of the pore-throat, greater heterogeneity, larger specific surface area, and the smaller the average pore-throat size, thereby providing a smaller pore space. Under such circumstances, the smaller the reservoir space provided by the sandstone for fluids is not conducive to the charging and accumulation of tight sandstone gas. $D_{m\text{-}t1}$ and $D_{m\text{-}t2}$ are negatively correlated with the final mercury saturation (Fig. 17b, c). It suggests the size of tight sandstone throats and their heterogeneity extremely affected the percolation and storage capacity of reservoir fluids. $D_{n\text{-}1}$ (Fig.17d) shows a significant negative correlation with movable fluid saturation. It demonstrates the larger the D of pore-throat, the greater heterogeneity, the more complicated microstructure, while the worse the seepage capacity of reservoir fluids.

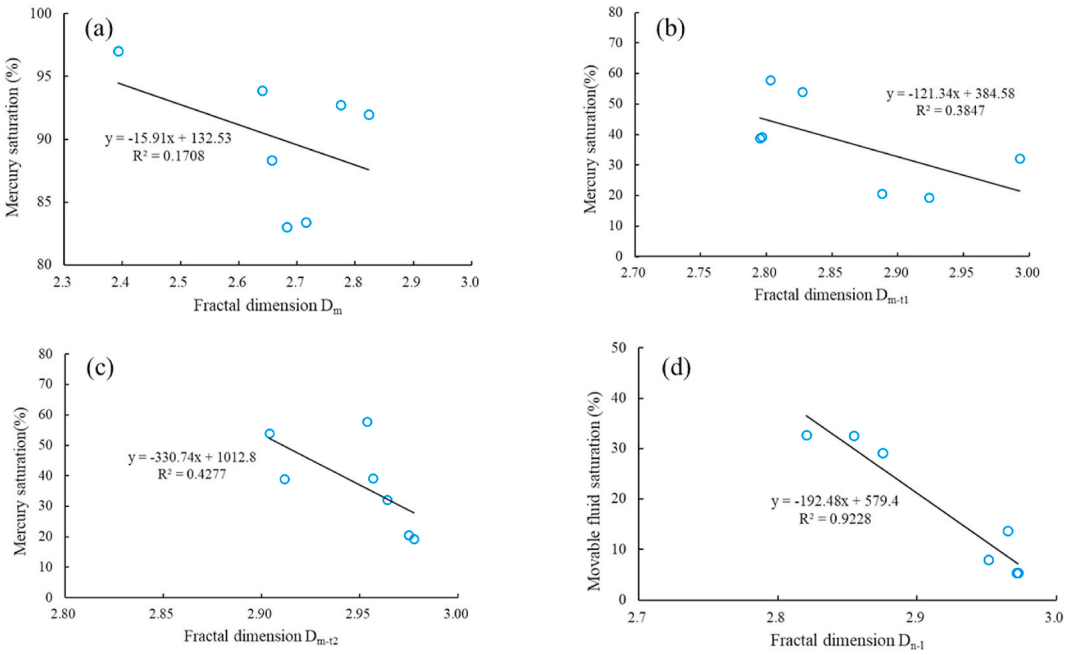

Fig.17. The plot of D_m, D_{m-t1}, and D_{m-t2}, D_{n-1} vs. mercury saturation (a)–(c), and movable fluid saturation (d).

Thus, the fluid resistance encountered during flowing through the network of pores and throats is greater, which is not conducive to the exploitation of tight gas in sandstones.

According to our research, the fractal theory is reliable, and it can better characterize the pore structure characteristics of ultra-low permeability reservoirs. Moreover, it plays an important role in evaluating reservoir quality and improving oil and gas recovery. This study analyzed and evaluated the influence of pores and throats of different sizes on reservoir quality and fluid flow-ability. The quality of the reservoir affects the amount of movable fluid. In the process of oil and gas field development, these two factors are considered the most important that can affect the final decision-making of producers to a large extent. Therefore, it is of great significance to explore the influence of different pore-throat combinations on the quality of the reservoir and the fluid flow-ability.

6. Conclusions

(1) The tight sandstone of Shihezi Formation in the Sulige area of Ordos Basin is quartzose sandstone with an average porosity and permeability of 11.58% and 0.25mD, respectively. The most common types of pores are residual intergranular pores and dissolved pores, followed by inter-crystalline pores and microcracks. The throat types are mainly tubular throats and sheet throats.

(2) By analyzing the limitations and advantages of experiments, this research synthesized the full-size PSD curve of the sample using HPMI and NMR. The full-size PSD curve presents bimodal and unimodal distribution characteristics, which is in good agreement with rock physical properties and movable fluid saturation.

(3) Three methods: HPMI, CRMI, and NMR are used to quantitatively study the complexity of pore-throat structure based on fractal theory. Different experimental techniques or interpretation models acquire different fractal dimensions. Comprehensive analysis shows the pore-throat of tight sandstone has fractal characteristics, and the throat has double-fractal characteristics. The development of the throat controls the reservoir capacity and fluid flow capacity.

(4) The correlation analysis between D_m, D_{m-t1}, D_{m-t2}, and physical properties show the larger the fractal dimension, the worse the reservoir physical properties. Moreover, the larger throat has a stronger control effect on the reservoir space and fluid seepage. Furthermore, mercury saturation, movable fluid saturation, and fractal dimension are negatively correlated, indicating the complicated pore-throat structure will reduce the permeability and destroy the free fluid storage space.

Author contributions

Yuping Wu: Conceptualization, Methodology, Data curation, Formal analysis, Writing-Original Draft, Writing - Review & Editing. **Chenglin Liu**: Supervision, Funding acquisition, Project administration, Visualization. **Siqi Ouyang**: Conceptualization, Validation, Writing-Review & Editing. **Bin Luo**: Data curation, Investigation. **Dingding Zhao**: Data curation, Investigation. **Wei Sun**: Resources, Project administration. **Rizwan Sarwar Awan**: Resources, Data curation, Writing-Original Draft. **Zhendong Lu**: Investigation. **Guoxiong Li**: Investigation. **Qibiao Zang**: Resources.

Declaration of competing interest

The authors declare that they have no known competing financial interests or personal relationships that could have appeared to influence the work reported in this paper.]

Acknowledgments

This research was financially funded by the Natural Science Foundation of China (Grant No. 41872127).

References

Brooks, R.H., Corey, A.T., 1964. Hydraulic Properties of Porous Media. Hydro Paper No.5. Colorado State University.

Clarkson, C.R., Freeman, M., He, L., Agamalian, M., Melnichenko, Y.B., Mastalerz, M., Bustin, R.M., Radliński, A.P., Blach, T.P., 2012. Characterization of tight gas reservoir pore structure using USANS/SANS and gas adsorption analysis. Fuel 95, 371–385.

Clarkson, C.R., Solano, N., Bustin, R.M., Bustin, A.M.M., Chalmers, G.R.L., He, L., Melnichenko, Y.B., Radliński, A.P., Blach, T.P., 2013. Pore structure characterization of North American shale gas reservoirs using USANS/SANS, gas adsorption, and mercury intrusion. Fuel 103, 606–616.
Curtis, M.E., Cardott, B.J., Sondergeld, C.H., Rai, C.S., 2012. Development of organic porosity in the Woodford Shale with increasing thermal maturity. Int. J. Coal Geol. 103, 26–31.
Dai, J., Ni, Y., Gong, D., Feng, Z., Liu, D., Peng, W., Han, W., 2017. Geochemical characteristics of gases from the largest tight sand gas field (Sulige) and shale gas field (Fuling) in China. Mar. Petrol. Geol. 79, 426–438.
Dong, X., Sun, J., Li, J., Gao, H., Liu, X., Wang, J., 2015. Experimental research of gas shale electrical properties by NMR and the combination of imbibition and drainage. J. Geophys. Eng. 12, 610–619.
Fan, A., Yang, R., Lenhardt, N., Wang, M., Han, Z., Li, J., Li, Y., Zhao, Z., 2019. Cementation and porosity evolution of tight sandstone reservoirs in the Permian Sulige gas field, Ordos Basin (central China). Mar. Petrol. Geol. 103, 276–293.
Friesen, W.I., Mikula, R.J., 1987. Fractal dimensions of coal particles. J. Colloid Interface Sci. 120, 263–271.
Golab, A.N., Knackstedt, M.A., Averdunk, H., Senden, T., Butcher, A.R., Jaime, P., 2010. 3D porosity and mineralogy characterization in tight gas sandstones. Lead. Edge 29, 1476–1483.
Guo, X., Huang, Z., Zhao, L., Han, W., Ding, C., Sun, X., Yan, R., Zhang, T., Yang, X., Wang, R., 2019. Pore structure and multi-fractal analysis of tight sandstone using MIP, NMR and NMRC methods: a case study from the Kuqa depression, China. J. Petrol. Sci. Eng. 178, 544–558.
Hu, Q., Ewing, R.P., Dultz, S., 2012. Low pore connectivity in natural rock. J. Contam. Hydrol. 133, 76–83.
Huang, H., Chen, L., Sun, W., Xiong, F., Ji, W., Jia, J., Tang, X., Zhang, S., Gao, J., Luo, B., 2018a. Pore-throat structure and fractal characteristics of Shihezi Formation tight gas sandstone in the Ordos Basin, China. Fractals 26.
Huang, H., Li, R., Jiang, Z., Li, J., Chen, L., 2020a. Investigation of variation in shale gas adsorption capacity with burial depth: insights from the adsorption potential theory. J. Nat. Gas Sci. Eng. 73.
Huang, H., Li, R., Xiong, F., Hu, H., Sun, W., Jiang, Z., Chen, L., Wu, L., 2020b. A method to probe the pore-throat structure of tight reservoirs based on low-field NMR: insights from a cylindrical pore model. Mar. Petrol. Geol. 117.
Huang, H., Sun, W., Ji, W., Zhang, R., Du, K., Zhang, S., Ren, D., Wang, Y., Chen, L., Zhang, X., 2018b. Effects of pore-throat structure on gas permeability in the tight sandstone reservoirs of the Upper Triassic Yanchang formation in the Western Ordos Basin, China. J. Petrol. Sci. Eng. 162, 602–616.
Hui, W., Wang, Y., Ren, D., Jin, H., 2020. Effects of pore structures on the movable fluid saturation in tight sandstones: a He8 formation example in Sulige Gasfield, Ordos Basin, China. J. Petrol. Sci. Eng. 192.
Kleinberg, R.L., Horsfield, M.A., 1990. Transverse relaxation processes in porous sedimentary rock. J. Magn. Reson. 88, 9–19.
Lai, J., Wang, G., 2015. Fractal analysis of tight gas sandstones using high-pressure mercury intrusion techniques. J. Nat. Gas Sci. Eng. 24, 185–196.
Lai, J., Wang, G., Cao, J., Xiao, C., Wang, S., Pang, X., Dai, Q., He, Z., Fan, X., Yang, L., Qin, Z., 2018. Investigation of pore structure and petrophysical property in tight sandstones. Mar. Petrol. Geol. 91, 179–189.
Li, A., Ren, X., Wang, G., Wang, Y., Jiang, K., 2015. Characterization of pore structure of low permeability reservoirs using a nuclear magnetic resonance method. J. China Univ. Petrol. 39, 92–98.
Li, K., 2010. Analytical derivation of Brooks–Corey type capillary pressure models using fractal geometry and evaluation of rock heterogeneity. J. Petrol. Sci. Eng. 73, 20–26.
Li, K., Horne, R.N., 2006. Fractal modeling of capillary pressure curves for the Geysers rocks. Geothermics 35, 198–207.
Li, P., Zheng, M., Bi, H., Wu, S., Wang, X., 2017. Pore throat structure and fractal characteristics of tight oil sandstone: a case study in the Ordos Basin, China. J. Petrol. Sci. Eng. 149, 665–674.
Li, Y., Wang, Z., Pan, Z., Niu, X., Yu, Y., Meng, S., 2019. Pore structure and its fractal dimensions of transitional shale: a cross-section from east margin of the Ordos Basin, China. Fuel 241, 417–431.
Li, Z., Shen, X., Qi, Z., Hu, R., 2018a. Study on the pore structure and fractal characteristics of marine and continental shale based on mercury porosimetry, N2 adsorption and NMR methods. J. Nat. Gas Sci. Eng. 53, 12–21.
Li, Z., Wu, S., Xia, D., He, S., Zhang, X., 2018b. An investigation into pore structure and petrophysical property in tight sandstones: a case of the Yanchang Formation in the southern Ordos Basin, China. Mar. Petrol. Geol. 97, 390–406.
Liu, D., Ren, D., Du, K., Qi, Y., Ye, F., 2021. Impacts of mineral composition and pore structure on spontaneous imbibition in tight sandstone. J. Petrol. Sci. Eng. 201.
Liu, D., Sun, W., Ren, D., Li, C., 2019. Quartz cement origins and impact on storage performance in Permian Upper Shihezi Formation tight sandstone reservoirs in the northern Ordos Basin, China. J. Petrol. Sci. Eng. 178, 485–496.
Ma, X., Guo, S., Shi, D., Zhou, Z., Liu, G., 2019. Investigation of pore structure and fractal characteristics of marine-continental transitional shales from Longtan Formation using MICP, gas adsorption, and NMR (Guizhou, China). Mar. Petrol. Geol. 107, 555–571.
Mandelbrot, B.B., 1983. The Fractal Geometry of Nature. Freeman, San Francisco.
Mayo, S., Josh, M., Nesterets, Y., Esteban, L., Pervukhina, M., Clennell, M.B., Maksimenko, A., Hall, C., 2015. Quantitative micro-porosity characterization using synchrotron micro-CT and xenon K-edge subtraction in sandstones, carbonates, shales and coal. Fuel 154, 167–173.
Morrow Norman, R., 1970. Physics and thermodynamics of capillary action in porous media. Ind. Eng. Chem. 62, 32–56.
Nie, R., Zhou, J., Chen, Z., Liu, J., Pan, Y., 2021. Pore structure characterization of tight sandstones via a novel integrated method: a case study of the Sulige gas field, Ordos Basin (Northern China). J. Asian Earth Sci. 213.
Nooruddin, H.A., Hossain, M.E., Al-Yousef, H., Okasha, T., 2014. Comparison of permeability models using mercury injection capillary pressure data on carbonate rock samples. J. Petrol. Sci. Eng. 121, 9–22.
Oluwadebi, A.G., Taylor, K.G., Ma, L., 2019. A case study on 3D characterisation of pore structure in a tight sandstone gas reservoir: the Collyhurst Sandstone, East Irish Sea Basin, northern England. J. Nat. Gas Sci. Eng. 68.
Ouyang, Z., Liu, D., Cai, Y., Yao, Y., 2016. Fractal analysis on heterogeneity of pore–fractures in middle–high rank coals with NMR. Energy Fuel. 30, 5449–5458.
Peng, L., Zhang, C., Ma, H., Pan, H., 2019. Estimating irreducible water saturation and permeability of sandstones from nuclear magnetic resonance measurements by fractal analysis. Mar. Petrol. Geol. 110, 565–574.
Qu, Y., Sun, W., Tao, R., Luo, B., Chen, L., Ren, D., 2020. Pore–throat structure and fractal characteristics of tight sandstones in Yanchang Formation, Ordos Basin. Mar. Petrol. Geol. 120.
Ren, D., Zhou, D., Liu, D., Dong, F., Ma, S., Huang, H., 2019. Formation mechanism of the upper triassic yanchang formation tight sandstone reservoir in Ordos Basin—take chang 6 reservoir in jiyuan oil field as an example. J. Petrol. Sci. Eng. 178, 497–505.
Schmitt, M., Fernandes, C.P., da Cunha Neto, J.A.B., Wolf, F.G., dos Santos, V.S.S., 2013. Characterization of pore systems in seal rocks using nitrogen gas adsorption combined with mercury injection capillary pressure techniques. Mar. Petrol. Geol. 39, 138–149.
Shao, X., Pang, X., Li, H., Zhang, X., 2017. Fractal analysis of pore network in tight gas sandstones using NMR method: a case study from the Ordos Basin, China. Energy Fuel. 31, 10358–10368.
Shen, P., Li, K., Jia, F., 1995. Quantitative description for the heterogeneity of pore structure by using mercury capillary pressure curves. In: SPE 29996, Proceedings of the SPE International Meeting Held in Beijing, China, November 14–17.
Sun, L., Zou, C., Jia, A., Wei, Y., Zhu, R., Songtao, W.U., Guo, Z., 2019. Development characteristics and orientation of tight oil and gas in China. Petrol. Explor. Dev. 46, 1015–1026.
Ufer, K., Stanjek, H., Roth, G., Dohrmann, R., Kleeberg, R., Kaufhold, S., 2008. Quantitative phase analysis of bentonites by the Rietveld method. Clay Clay Miner. 56, 272–282.
Wang, F., Cheng, Y., Lu, S., Jin, K., Zhao, W., 2014. Influence of coalification on the pore characteristics of middle high rank coal. Energy Fuels 28, 5729–5736.
Wang, M., Tang, H., Zhao, F., Liu, S., Yang, Y., Zhang, L., Liao, J., Lu, H., 2017. Controlling factor analysis and prediction of the quality of tight sandstone reservoirs: a case study of the He8 Member in the eastern Sulige Gas Field, Ordos Basin, China. J. Nat. Gas Sci. Eng. 46, 680–698.
Washburn, E.W., 1921. The dynamics of capillary flow. Phys. Rev. 17, 273–283.
Wu, H., Zhao, J., Wu, W., Li, J., Huang, Y., Chen, M., 2021. Formation and diagenetic characteristics of tight sandstones in closed to semi-closed systems: typical example from the Permian Sulige gas field. J. Petrol. Sci. Eng. 199.
Xiao, D., Lu, S., Lu, Z., Huang, W., Gu, M., 2016. Combining nuclear magnetic resonance and rate-controlled porosimetry to probe the pore-throat structure of tight sandstones. Petrol. Explor. Dev. 43, 961–970.
Xiao, H., Liu, R.e., Zhang, F., Lin, C., Zhang, M., 2019. Sedimentary model reconstruction and exploration significance of permian He 8 member in Ordos Basin, NW China. Petrol. Explor. Dev. 46, 280–292.
Yang, H., Liu, X., 2014. Progress in paleozoic coal-derived gas exploration in the Ordos Basin, west China. Petrol. Explor. Dev. 41, 144–152.
Yang, H., Liu, X., Yan, X., 2015. The relationship between tectonic-sedimentary evolution and tight sandstone gas reservoir since the late Paleozoic in Ordos Basin, 22 (3), 174–183.
Yang, R., Fan, A., Van Loon, A.J., Han, Z., Wang, X., 2014. Depositional and diagenetic controls on sandstone reservoirs with low porosity and low permeability in the eastern Sulige gas field, China. Acta Geol. Sinica Engl. Ed. 88, 1513–1534.
Yao, Y., Liu, D., Che, Y., Tang, D., Tang, S., Huang, W., 2010. Petrophysical characterization of coals by low-field nuclear magnetic resonance (NMR). Fuel 89, 1371–1380.
Yuan, H.H., Swanson, B.F., 1989. Resolving pore-space characteristics by rate-controlled porosimetry. SPE Form. Eval. 4, 17–24.
Zhang, F., Jiang, Z., Sun, W., Li, Y., Zhang, X., Zhu, L., Wen, M., 2019. A multiscale comprehensive study on pore structure of tight sandstone reservoir realized by nuclear magnetic resonance, high pressure mercury injection and constant-rate mercury injection penetration test. Mar. Petrol. Geol. 109, 208–222.
Zhang, F., Jiang, Z., Sun, W., Zhang, X., Zhu, L., Li, X., Zhao, W., 2020. Effect of microscopic pore-throat heterogeneity on gas-phase percolation capacity of tight sandstone reservoirs. Energy Fuel. 34, 12399–12416.
Zhang, Z., Weller, A., 2014. Fractal dimension of pore-space geometry of an Eocene sandstone formation Fractal dimension of pore-space geometry. Geophysics 79, 377–387.
Zhao, H., Ning, Z., Wang, Q., Zhang, R., Zhao, T., Niu, T., Zeng, Y., 2015. Petrophysical characterization of tight oil reservoirs using pressure-controlled porosimetry combined with rate-controlled porosimetry. Fuel 154, 233–242.
Zhao, J., Zhang, W., Li, J., Cao, Q., Fan, Y., 2014. Genesis of tight sand gas in the Ordos Basin, China. Org. Geochem. 74, 76–84.
Zhou, L., Kang, Z., 2016. Fractal characterization of pores in shales using NMR: a case study from the lower cambrian niutitang Formation in the middle yangtze platform, southwest China. J. Nat. Gas Sci. Eng. 35, 860–872.

Zhou, S., Liu, D., Cai, Y., Yao, Y., 2016. Fractal characterization of pore–fracture in low-rank coals using a low-field NMR relaxation method. Fuel 181, 218–226.
Zhu, F., Hu, W., Cao, J., Sun, F., Liu, Y., Sun, Z., 2018. Micro/nanoscale pore structure and fractal characteristics of tight gas sandstone: a case study from the Yuanba area, northeast Sichuan Basin, China. Mar. Petrol. Geol. 98, 116–132.
Zou, C., Zhu, R., Liu, K., Su, L., Bai, B., Zhang, X., Yuan, X., Wang, J., 2012. Tight gas sandstone reservoirs in China: characteristics and recognition criteria. J. Petrol. Sci. Eng. 88-89, 82–91.